Acta Materialia 154 (2018) 237–245

Contents lists available at ScienceDirect

Acta Materialia

journal homepage: www.elsevier.com/locate/actamat

Full length article

Mechanical properties of sprayed overlayers on superalloy substrates, obtained via indentation testing

J.E. Campbell [a], T. Kalfhaus [b], R. Vassen [b], R.P. Thompson [a], J. Dean [a], T.W. Clyne [a, *]

[a] Department of Materials Science & Metallurgy, Cambridge University, 27 Charles Babbage Road, Cambridge CB3 0FS, UK
[b] Forschungszentrum Jülich GmbH, 52425 Jülich, Germany

ARTICLE INFO

Article history:
Received 12 May 2018
Received in revised form
17 May 2018
Accepted 18 May 2018
Available online 22 May 2018

Keywords:
Indentation
Inverse FEM
Superalloy
Plasma spraying

ABSTRACT

This paper concerns the use of a recently-developed methodology for inferring stress-strain curves from indentation data, based on iterative FEM simulation of the procedure. A relatively large indenter (2 mm diameter) is used, with deep penetration (to about 25% of the indenter radius). This has been carried out on (polished) free surfaces of sprayed superalloy overlayers on single crystal superalloy substrates. Both load-displacement data and residual indent profiles were obtained, with the overlayers being in two different conditions (as-sprayed and annealed). The overlayers were relatively thick (~2.5 mm), so it was also possible to carry out uniaxial compression tests on them (in the through-thickness direction). The inferred stress-strain curves were similar in each case when derived from load-displacement data and indent profiles, and also close to the plots obtained by conventional uniaxial testing. The yield stress levels in both cases were around 1000 MPa, but the work hardening rate was significantly higher for the as-sprayed material. This kind of information is of considerable potential value when attempting to optimize the properties of such overlayers. The procedure can be employed, with some confidence, to cases for which uniaxial testing is difficult or impossible.

1. Introduction

There is keen interest in the degradation of components in gas turbines, particularly within and beyond the combustion chamber, relating to turbines for both power generation (Industrial Gas Turbines – IGTs) and aero-engines. Materials in these environments often require good resistance to creep, but they may also be prone to oxidation, cracking, pitting, erosion and other types of damage. Such degradation [1–8] can be accelerated by certain species, such as NaCl from ingested air and S from either the fuel or the air, leading to formation of low melting point compounds such as sodium sulphate (Na_2SO_4). There are industrial drivers towards conditions involving greater ingestion of such species and/or higher operating temperatures, creating a need for improved understanding of the phenomena involved and for practical measures to combat these problems. It's also worth noting that the use of single crystal components (such as turbine blades), which has been common for some time in aeroengines, has over recent years become more popular in IGTs.

Components such as blades can, of course, be replaced, but this is an expensive and time-consuming operation. An attractive option is that of repair. This is aimed at removing serious defects, such as cracks, and also at replacing metal lost by oxidation, erosion or other degradation mechanisms. It's clear that such deposited material must have very similar thermo-mechanical properties to those of the substrate, and must also be very well bonded to it, if the repaired component is to perform well.

There has been extensive work on development of such procedures. In particular, a lot of effort [9–12] has been directed towards laser processing of superalloy powders located on the substrate, often with the specific objective of forming single crystals (epitaxial with the substrate). While the outcomes of such studies have often appeared promising, this route does present certain problems, often associated with the very high thermal gradients that tend to be produced during such processing. Furthermore, porosity levels can be high and in general the microstructure is often very different from that of the (directionally solidified) substrate.

Other approaches [13,14] have involved various kinds of welding or brazing operation, using gas combustion or electric arcs as the heat source. These procedures tend to create very inhomogeneous

* Corresponding author.
E-mail address: twc10@cam.ac.uk (T.W. Clyne).

https://doi.org/10.1016/j.actamat.2018.05.043

structures, and often leave high levels of residual stress. There have also been studies [15,16] of the use of EB-PVD for this purpose, although this is a slow process, requiring a vacuum, and is not really very well suited to the creation of relatively thick over-layers.

A further option is to use a spraying technique, offering the potential for good control over coating thickness and microstructure. There has been some work [17,18] on cold spraying of superalloy powders, aimed at substrate repair, but in general the associated levels of porosity, and the relatively poor bonding between particles, mean that it is very difficult to create suitable microstructures. However, thermal spraying, specifically plasma spraying, is potentially attractive. This process is, of course, widely used to create ceramic coatings on components such as turbine blades, particularly for thermal barrier purposes. The necessary technology is thus already well established in the turbine industry. There is also scope for creating a high substrate surface temperature during the process, promoting directional solidification and improving the chances of epitaxial growth.

However, while there has been work [19,20] on plasma sprayed metallic over-layers of various kinds (mostly for oxidation protection), study of plasma sprayed superalloy layers for repair purposes has been limited. Okazaki et al. [21] did investigate such repair of CMSX-4, although this was in the rather specialized context of compensating for loss of certain elements in order to counter an associated reduction in fatigue life, rather than aiming to produce a surface layer with a microstructure very similar to that of the substrate. It is therefore timely to undertake a detailed study of the potential of this approach, particularly in terms of control over the microstructure and properties of the over-layer.

Of course, a major challenge in attempting to optimize such layers lies in studying their mechanical properties (such as plasticity parameters), which are central to an assessment of their suitability. Conventional testing of layers that are likely to be no more than 1 mm or so in thickness is certainly not easy. An attractive concept under these circumstances is to use instrumented indentation. This is an experimentally versatile technique that can readily be applied to small samples, including overlayers, and can be used to map properties over a surface. The main difficulty here is that, while indentation is routinely used to obtain a hardness value, this is not a "genuine" property, although it is a yardstick related to the resistance to plastic deformation (and depends on both yield stress and work hardening characteristics). While it may be of interest to measure the hardness of superalloy overlayers, in order to make a comparison of sorts with substrate values, what is really required here is a capability to infer a (uniaxial) stress-strain curve for the coating from indentation data.

In fact, this objective is being energetically pursued at present. The approaches used fall into two main categories. Many studies have sought to identify analytical formulations that can be applied to the experimental data (mostly load-displacement curves). This has obvious attractions, since such a formulation, even if involving relatively complex expressions and algorithms, would allow rapid extraction of the stress-strain curves via a well-defined path. Unfortunately, the stress and strain fields beneath an indenter, even one with a simple shape such as a sphere, are complex and change with penetration depth, making it difficult to identify realistic analytical relationships.

Of course, for a material with a given (uniaxial) stress-strain curve, assumed to be applicable to deviatoric (von Mises) components of stress and strain for multi-axial situations, the load-displacement plot during indentation can be predicted (using FEM), for any given indenter shape. However, the inverse problem of inferring the stress-strain relationship from such a load-displacement plot is much more challenging, with considerable scope for ambiguity (different stress-strain relationships giving effectively the same load-displacement plot). In fact, this problem is the main obstacle for the second category of approach [22–29], which is simply to carry out iterative FEM modeling of the indentation process using various trial stress-strain curves (characterized via a set of parameter values) and aim to converge on the set giving optimum agreement with the experimental load-displacement plot. This is at least a transparent and rigorous procedure, although its wide implementation is currently inhibited by the need to carry out FEM modeling runs that are specific to each individual case, as well as by the "uniqueness" problem.

However, recent work [30,31] has shown that it is in fact possible to converge on best-fit sets of plasticity parameter values quite efficiently, using a spherical indenter and penetrating to a significant depth (δ/R ~20–40%, where δ is the depth and R is the radius of the indenter). Software has been developed that incorporates algorithms for automated convergence. Further details are available elsewhere. This is used in the current work. The issue of ensuring that a representative volume is being interrogated is an important one here, since many of the samples (overlayers) have a relatively large grain size (but are not single crystals). A relatively large indenter diameter (2 mm) was therefore chosen for this work. This meant that the substrate needed to be incorporated into the modeled domain.

2. Experimental procedures

2.1. Materials and specimen production

The substrates were of ERBO-1 and the powder was CMSX-4. Their compositions are presented in Table 1, where it can be seen that these two alloys have very similar specifications. A set of samples was produced by vacuum plasma spraying, using the conditions specified in Table 2. The VPS is a Plasma Technik facility, with a F4VB gun and a nozzle diameter of 7 mm. The powder was injected radially at the front of the nozzle. Substrate dimensions were 32 × 20 × 2.5 mm, with a hole of 1.1 mm diameter to locate a (k-type) thermocouple. The substrate surface was polished down to a 3 μm finish, using diamond paste. As indicated in Table 2, the substrate temperature was controlled during deposition. This was done largely via the use of a 1 kW electrical resistance heater (with a doped Si_3N_4 element). In view of the importance of avoiding substrate oxidation prior to spraying, initial heating was carried out using the (H_2-containing) plasma plume, which provided a reducing atmosphere. This was done immediately prior to spraying, with the substrate temperature during the process being largely controlled via the heater setting. In the work described here, the substrate temperature was held at 1000 °C. The post-spraying heat treatment referred to in Table 2 as an anneal was a period 6 h at 1315 °C. At the end of this treatment, samples were quenched.

2.2. Microstructural examination

Samples were prepared for both optical and SEM examination by polishing down to 1 μm diamond and then finishing with 50 nm colloidal silica suspension, which had a pH of about 10 and generated an etching effect. SEM images were obtained in BSE

Table 1
Nominal compositions of the CMSX-4 and ERBO-1 alloys.

Alloy	Composition (wt.%)									
	Cr	Co	Mo	Al	Ti	Ta	Hf	W	Re	Ni
CMSX-4 (powder)	6.4	9.5	0.6	6.0	0.9	8.5	0.1	8.1	2.9	bal.
ERBO-1 (substrate)	6.5	9.6	0.6	5.7	1.0	6.5	0.1	6.4	2.9	bal.

Table 2
Spraying and heat treatment conditions employed.

Sample Code	Plasma power (kW)	Chamber pressure (mbar)	Plasma gas flow rates ($l\,min^{-1}$)	Stand-off distance (mm)	Powder size (μm)	Substrate T (°C)	Overlayer thickness (mm)	Heat treatment
A1	46	60	Ar 50, H_2 10	300	22–45	1000	2.5	–
A2	446	60	Ar 50, H_2 10	300	22–45	1000	2.5	Anneal

mode, with an accelerating voltage of 5 kV and a working distance of 3–6 mm, using either a Hitachi TM3000 or a FEI Phenom-Pure machine.

2.3. Uniaxial testing

Conventional uniaxial testing (in compression) was carried out at room temperature (22 °C ±2 °C), using an Instron 3367 screw-driven testing machine. A load cell with a capacity of 30 kN was employed. Testing was carried out under displacement control, at a rate of 10 μm s^{-1}. Samples, which were cut to shape using Electro-Discharge Machining (EDM), were cuboids with a length in the testing direction of 2.5 mm (the coating thickness) and a square section of side 3.5 mm. Tests took about 30 s and the strain rate was of the order of 10^{-3} s^{-1}. Both stress and strain levels were converted from nominal to true values for comparison with indentation-derived curves. Samples were compressed between rigid (hardened steel) platens, using MoS_2 lubricant to minimize barreling. In practice, there will always be at least some friction between sample and platen, which could possibly have an effect on the stress-strain curve (cause a rise in the apparent work hardening rate), particularly at relatively high strains (>~10%). However, in the current work this effect was probably small. The displacement was measured using an eddy current gauge having a resolution of about ±0.25 μm. It was attached to the upper platen and actuated against the lower one. Any error arising from (elastic) deformation of the platens is unlikely to be significant and there was no need for any compliance calibration.

2.4. Indentation testing

Indentation was carried out in the through-thickness direction, on free surfaces of samples, which were first polished down to 1 μm. Testing was carried out with the same machine, and under similar conditions, to those used for uniaxial testing. A spherical indenter of radius 1 mm was employed, made of a WC-Co cemented carbide. This sphere was located in a matching recess in a steel housing, where it was secured by brazing. The set-up is depicted in Fig. 1. Compliance calibration was needed, since it's important in work of this type that the displacement data should be obtained under conditions that correspond closely to those being simulated in the model. The compliance was measured by pushing the indenter into a matched recess (about 500 μm deep) in a 5 mm thick plate of alumina, the recess having been created via abrasive rotational honing with the same type of indenter as that used in the tests. After a short bedding-down regime, this gave a linear plot (ie constant compliance) and this gradient was subtracted from indentation load-displacement plots. (The contribution to the compliance from the alumina plate itself is considered to be negligible.)

This calibration coped with the compliance of the housing, including the braze layer between indenter and housing, and also that of the top half of the indenter. (It would also cope with the compliance of other parts of the loading train, in cases for which that was significant). However, it did not compensate for the (elastic) deformation of the bottom half of the indenter, which could be significant in the early stages of indentation (when the contact area is small and the stresses and strains in the indenter could be relatively large). This part of the indenter was therefore included in the modeled domain, as shown in Fig. 1. This has the minor advantage that stresses in the indenter are being monitored, so it is possible, for example, to check on whether there might be any danger of it undergoing plastic deformation. The compliance measured in this way was fairly small (~5 μm kN^{-1}), so this was only a relatively minor correction.

The load was taken up to about 8 kN, typically generating a displacement (penetration) of about 250 μm ($\delta/R \sim 25\%$) and an indent diameter of around 1 mm. It was confirmed that the deformed region comprised a large number of grains in all cases, constituting a representative volume - see §4.1.

2.5. Residual indent topography

A Taylor Hobson (Talysurf) profilometer (ie a contacting stylus), with a wide-range inductive gauge and 2 μm radius cone recess tip, was used to measure residual indent profiles. Scans were carried out in two perpendicular directions, both through the central axis of the indent. The height resolution of these scans is about 2 μm. Tilt correction functions were applied to the raw data, based on the far-field parts of the scan being parallel. The average profile from the two orthogonal scans was used for comparison with predicted profiles.

3. Iterative FEM modeling

3.1. Constitutive plasticity law

For any approach involving iterative simulation of a deformation process, the stress-strain relationship (material plasticity response) must be characterized via a (small) set of parameter values. In fact, several expressions are in common use, but the most popular is the one often termed the Ludwik-Hollomon equation [32].

$$\sigma = \sigma_Y + K\varepsilon_P^n \quad (1)$$

where σ is the (von Mises) applied stress, σ_Y is its value at yield, ε_p is the plastic (von Mises) strain, K is the work hardening coefficient and n is the work hardening exponent. A power law of this type is consistent with strain hardening being mainly caused by the increasing density of dislocations (impairing their mobility as more jogs, tangles etc are formed), but with a hardening rate that falls off with continued straining (as the dislocation density approaches a saturation level).

3.2. FEM formulation, meshing and boundary conditions

An axi-symmetric FEM model was employed, based on the mesh illustrated in Fig. 1. There are about 5000 vol elements, all second order quadrilateral and/or triangular. The mesh was refined in regions of the sample close to the indenter, as shown. Sensitivity analyses confirmed that the meshes employed were sufficiently fine to achieve convergence, numerical stability and mesh-independent results. The complete sample was included in the

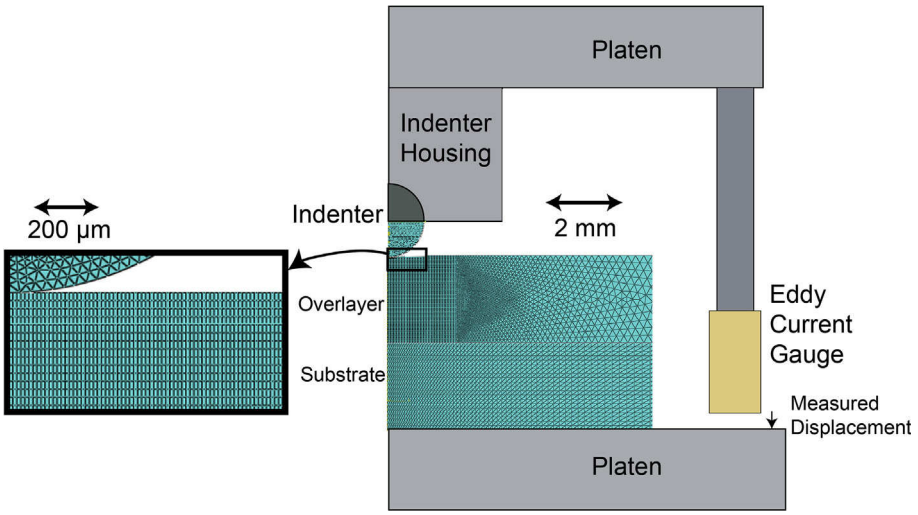

Fig. 1. Schematic of the indentation testing set-up, showing the mesh used in the FE model.

simulation, with its lower surface rigidly fixed in place. In modeling the complete sample, contributions to the displacement caused by its elastic deformation, as well as plastic deformation, are fully captured.

The effect of interfacial friction is routinely simulated via a coefficient of friction, μ, such that sliding between the two surfaces requires a shear stress, τ, given by

$$\tau = \mu\sigma_{\mathrm{n}} \tag{2}$$

where σ_{n} is the normal stress at the interface. The value of μ is expected to depend on the surface roughness of indenter and sample, and cannot be predicted *a priori*. It may also be noted that new sample surface is created during indentation. Modeling experience showed that the predicted behavior can have some sensitivity to the value, particularly as the penetration ratio starts to become relatively large (>~10%). The value of μ was therefore regarded as adjustable, so as to allow improvement of the fit between experimental and predicted load-displacement plots.

All material properties were assumed to be isotropic. For the overlays, this is expected to be a good approximation, since they are all polycrystalline (with a large number of grains) and, while some texture is expected, EBSD studies indicated that it was not strong. (While the columnar grains within the splats probably grew in <100> directions, splat orientations were fairly random - see §4.1 - so these coatings are probably close to being untextured.) The Young's modulus of this type of alloy [33] [34], does vary substantially with crystallographic direction (from about 135 GPa in <100> to about 310 GPa in <111>). For the overlays, an average value of 220 GPa was assumed. (The Poisson ratio varies much less, and is also much less significant in terms of modeling outcomes: a value of 0.25 was assumed.)

The substrate, on the other hand, is a single crystal, with two <100> directions lying in the plane of the free surface and the third one normal to it. Clearly, it exhibits pronounced elastic (and plastic) anisotropy. The assumption was made that it was elastically isotropic, with a Young's modulus of 130 GPa. This will only be acceptable if its elastic deformation is both small and approximately uniaxial (in <100>). This is expected to be valid for the current work. Furthermore, it was essential to avoid plastic deformation of the substrate, which would quickly become strongly anisotropic. These requirements effectively imposed a limit on the depth to which indentation could be carried out. It was decided that δ could be no greater than about 250 μm, representing about 10% of the coating thickness. Since the indenter radius was 1 mm, the value of δ/R is about 25%. In terms of obtaining reliable information about the work hardening behavior (§1), this is regarded as acceptable, although a higher value would have been preferable.

It may be noted at this point that it is, of course, perfectly possible for substrate plasticity to be incorporated into this type of model (with its plasticity parameters known). In the present case, however, the strong plastic (in-plane) anisotropy that would be exhibited by the substrate would mean that the radial symmetry would be lost and the modeling would need to be carried out in 3-D. In view of the large number of modeling runs involved in this approach, the associated computing time overhead was considered unacceptable for present purposes.

Trial FEM runs were used to confirm that these conditions would be suitable, and to explore issues such as the range of plastic strain likely to be generated in the samples. A typical outcome is shown in Fig. 2, where it can be seen that, for the penetration depth being used, the (von Mises) stress levels created in the substrate should be below those expected to stimulate plastic deformation. It can also be seen that the plastic strains in the overlayer range up to about 40%, which should give fairly good sensitivity to the work hardening characteristics. The stress level in the indenter is predicted to be high (~5 GPa), but this is below the expected yield stress of the cermet used and it was confirmed experimentally that it underwent no detectable plastic deformation during indentation.

3.3. Convergence procedure

The efficiency with which an optimized set of parameter values can be obtained is a key issue for this methodology. Procedures are required both to quantify the goodness-of-fit between predicted and target (experimental) indentation outcomes and to converge in parameter space on the location where this fit is maximized. In the current work, a least squares regression approach [35] has been used, aiming to minimize the sum of the squares of the residuals (differences between expected and modeled values of the variable). The goodness-of-fit is characterized by a parameter S_{red}, a dimensionless positive number that tends to zero as the fit becomes perfect. The best-fit set of values is obtained by iterative improvement, using a search algorithm. The algorithm used in the current work is the Nelder-Mead simplex search [36], as implemented by Gao and Han [37]. The algorithm is terminated once a specified

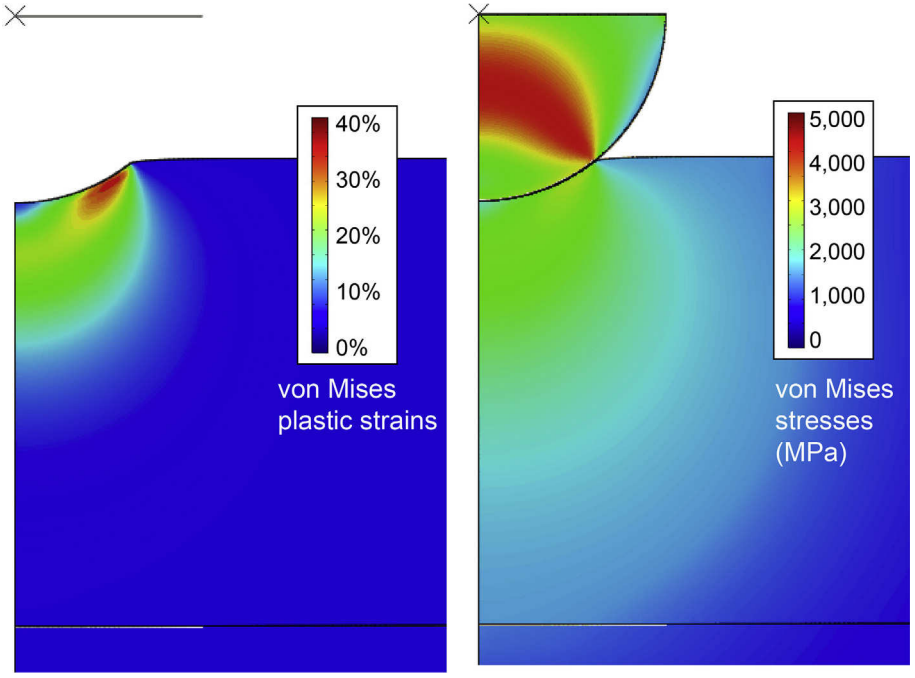

Fig. 2. Predicted fields of the von Mises plastic strain and the von Mises stress, using plasticity parameter values of $\sigma_Y = 1150$ MPa, K = 2400 MPa and n = 0.8, for a δ/R value of 25%.

convergence criterion has been met. The number of iterations to achieve convergence depends on a number of factors, in addition to this criterion specification. It has been found that the algorithm performs well in the present context. Full details are available elsewhere [31], but Appendix I outlines the procedures involved. In the present work, convergence operations were carried out separately on both load-displacement plots and residual indent profiles.

4. Characterisation of overlayers

4.1. Microstructural features

SEM micrographs of transverse sections from these two samples are shown in Fig. 3. It can be seen that, in the as-sprayed condition (Fig. 3(a)), these overlays comprise a large number of splats, each containing columnar grains grown through the thickness of the splat. The average grain size is thus quite small (~few μm). Also evident in this micrograph is the nature of the inter-splat porosity. The porosity level is typically expected to be ~10% in a sprayed metallic coating and this is approximately the level visible here (although examination of polished sections is often a rather unreliable method of assessing pore contents). Another feature apparent in Fig. 3(a) is the presence of a small amount of TCP phase (visible as small white inter-granular precipitates). These are more likely to form when the cooling rate is slow, as it was for these as-sprayed samples (on heated substrates).

It can be seen from Fig. 3(b) that the annealing treatment lead to recrystallization, possibly followed by some grain growth. This produced an equiaxed structure, with a grain size of ~50–100 μm. The presence of annealing twins constitutes clear evidence of recrystallization. It can also be seen that a relatively high level of porosity persisted in this sample, although there has been some rounding of individual pores (as a consequence of sintering effects) and possibly the pore content has been reduced somewhat. It's also noticeable that the TCP (white) phases are no longer present. This is consistent with the high cooling rate that was imposed after the

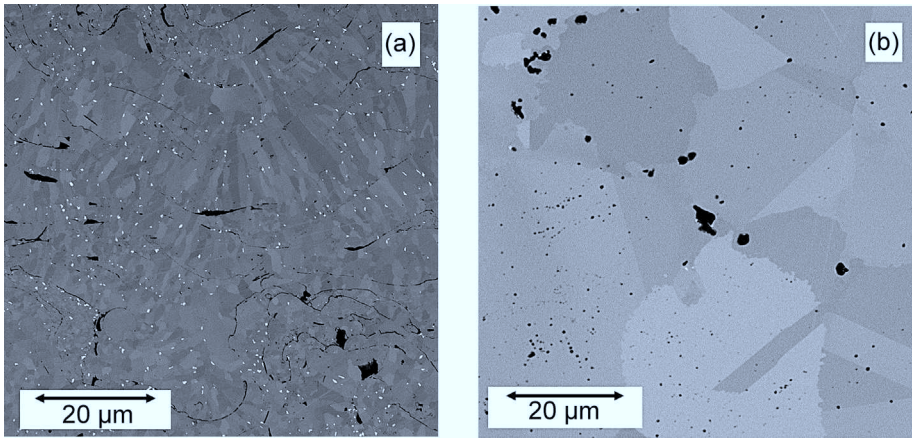

Fig. 3. SEM micrographs of transverse sections of overlays for (a) A1 (as-sprayed), and (b) A2 (annealed) samples.

annealing treatment.

The two corresponding optical micrographs in Fig. 4 cover substantial proportions of the overlayer thicknesses, showing that the grain structures are fairly uniform throughout (although it is too fine to resolve clearly at this magnification in the as-sprayed case). It can also be seen in these micrographs that the interfacial contact (adhesion of the overlays to the substrate) appears to be good. This is certainly no evidence of excessive porosity or oxide layers in this region. (The avoidance of substrate oxidation did require care - see §2.1 above.)

It was confirmed that the deformed regions around indents did in all cases constitute representative volumes - or at least that they contained many grains. This can be seen in Fig. 5, which shows a transverse section taken from near to the axis of an indent. In fact, since the indent depths were 250 μm, and the apparent depth of this one is about 100 μm, it's clear that this section is a little way from the axis, but even in this vicinity there are many grains being deformed.

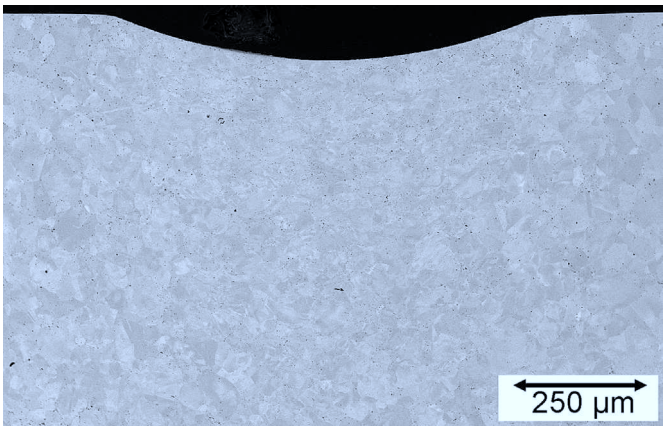

Fig. 5. Optical micrograph of a transverse section from sample A2, near the axis of an indent.

4.2. Inferred plasticity characteristics

The Nelder-Mead convergence algorithm [31] was applied to both the load-displacement plots and the residual indent shapes, for both types of sample. It was found that a value for the friction coefficient, μ, of 0.3 gave the best overall consistency. The progress of the algorithm, for the load-displacement plot of the as-sprayed material, is shown in Fig. 6, where it can be seen that convergence required about 60 iterations. This was typical of all of the runs. A comparison is shown in Fig. 7 between the two stress-strain curves inferred in this way, for each type of sample, and the corresponding plots obtained by direct uniaxial testing. It should be emphasized at this point that the latter should not be regarded as highly accurate, since such tests are difficult to carry out when sample dimensions are constrained to be very small, as in this case. Nevertheless, the level of agreement observed in this figure is in general very good. The sets of Ludwik-Hollomon parameter values obtained in this way are shown in Table 3.

It's certainly clear that, while both overlayers have relatively high yield stresses, it is not acceptable to neglect work hardening (as is effectively done when converting a hardness number to a yield stress). In fact, Vickers hardness tests were carried out on both types of sample, leading to H_V numbers (0.5 kg load) for the as-sprayed and annealed material of 542 and 475 kgf mm^{-2}, with a scatter of around ±10 kgf mm^{-2} in both cases. Using the standard relationship of $\sigma_Y \sim H_V/3$ (with H_V expressed in MPa), this leads to yield stress values of about 1.77 and 1.55 GPa. These would clearly be very misleading. Of course, a yield stress obtained from a hardness measurement should never be regarded as better than semi-quantitative.

An idea of the level of agreement obtained between measured and modeled indentation outcomes can be obtained from Figs. 8 and 9, which compare the load-displacement plots and the residual indent shapes that were obtained experimentally with the corresponding (optimized) model predictions. It can be seen that the agreement is good in all cases. (This can be quantified by the converged S_{red} values, which are recorded in Table 3: values of this parameter below 10^{-3} are considered acceptable and these values are all around 10^{-4}.) While the parameter sets obtained from load-displacement plots and from the profiles are not identical in either case, they correspond to very similar stress-strain curves and also agree well with the uniaxial data (Fig. 7). In general, it is clear that this methodology has the potential to obtain stress-strain plots in which a high level of confidence can be placed, particularly if both load-displacement data and residual indent profiles are used (although it would certainly be acceptable in most cases to use only one type of dataset). Of course, these measurements do need to be made to an appropriate level of accuracy and reproducibility.

5. Conclusions

The following conclusions can be drawn from this work:

(a) The methodology of iterative FEM simulation of the indentation process, with systematic comparison between experimental and predicted outcomes, has been applied to (polycrystalline) superalloy coatings produced on (single crystal) superalloy substrates. Such coatings are of interest in view of their potential use for repair of damaged turbine blades. They have been investigated mechanically in both as-

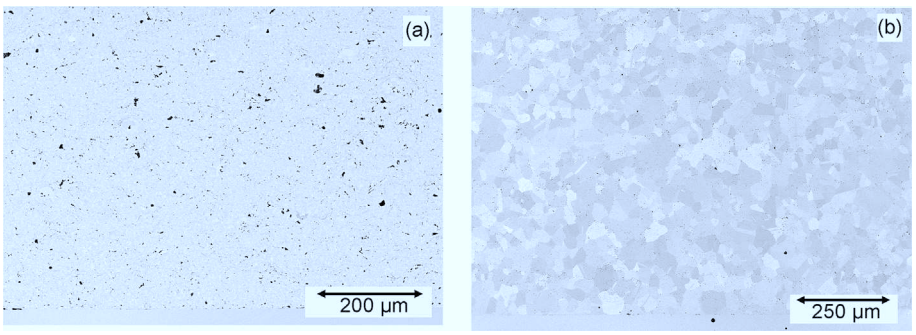

Fig. 4. Optical micrographs of transverse sections of overlays for (a) A1 (as-sprayed), and (b) A2 (annealed) samples.

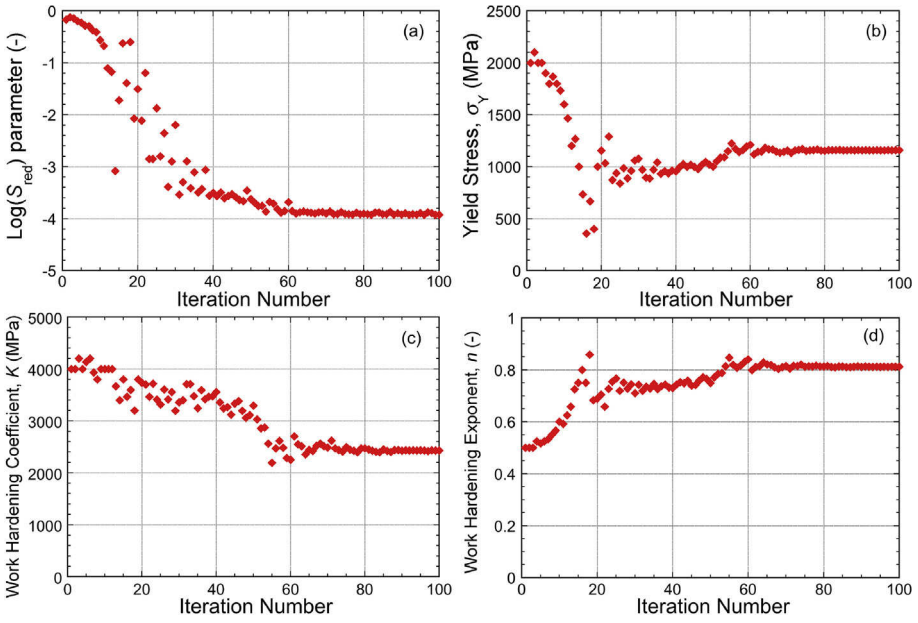

Fig. 6. Nelder-Mead convergence on an optimal (Ludwik-Hollomon) parameter set, targetting the load-displacement plot from indentation of sample A1, showing the evolution with iteration number of: (a) the goodness-of-fit parameter, S_{red}, (b) yield stress, (c) work hardening coefficient and (d) work hardening exponent.

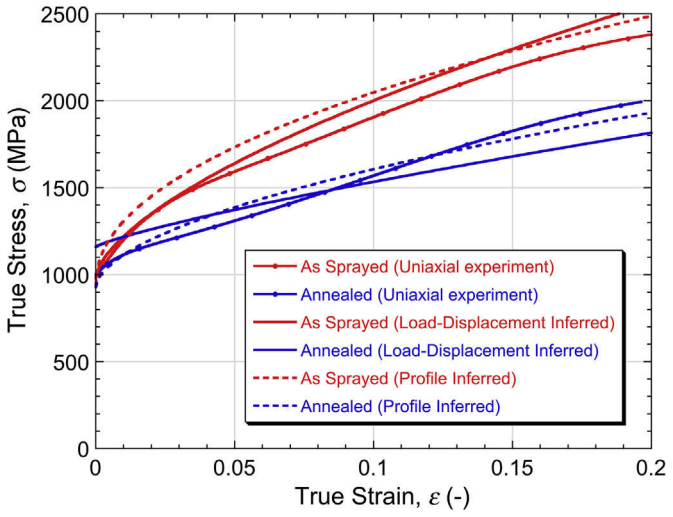

Fig. 7. Comparison between stress-strain curves obtained in conventional uniaxial compression tests and via indentation, for both sample conditions, inferred from either load-displacement plots or from residual indent profiles.

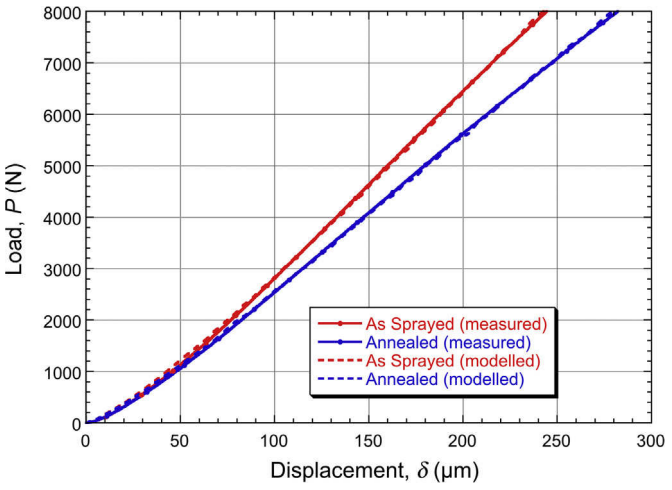

Fig. 8. Comparison between measured and predicted load-displacement plots, for both sample conditions.

Table 3
Inferred plasticity parameter values for both samples, for both types of target dataset.

Parameter	Sample A1 (as-sprayed)		Sample A2 (annealed)	
	From $P(\delta)$ data	From $\delta(r)$ data	From $P(\delta)$ data	From $\delta(r)$ data
Yield stress σ_Y (MPa)	978	945	1160	929
Work hardening coefficient, K (MPa)	4345	3370	2422	2489
Work hardening exponent, n (−)	0.629	0.485	0.811	0.565
Misfit parameter, S_{red} (−)	$10^{-3.8}$	$10^{-3.9}$	$10^{-3.9}$	$10^{-4.1}$

sprayed and annealed conditions. A large (2 mm diameter) spherical indenter was used, with a penetration depth of about 250 μm. (Deeper penetration might have been helpful, but it was capped at this level in order to avoid plastic deformation of the substrate.)

(b) Using the Ludwik-Hollomon plasticity law to simulate the stress-strain characteristics of the coatings, best fit values of the parameters in this equation have been obtained, with either load-displacement or residual indent shape data being used as target outcomes, for both types of sample. Searching

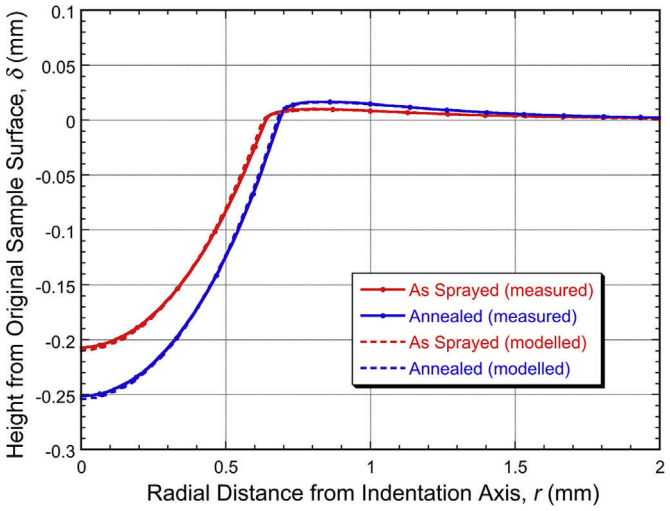

Fig. 9. Comparison between measured and predicted residual indent shapes, for both sample conditions.

of the 3-D parameter space for the location where predicted and modeled outcomes match most closely was done using a Nelder-Mead convergence algorithm. The friction coefficient, μ, during indentation also needs to be evaluated and a value of 0.3 was found to give the most consistent results.

(c) The main outcome was that inferred stress-strain curves were very similar when they were derived from load-displacement plots and from residual indent shapes, for both types of sample. The annealing operation caused appreciable softening, although the change was mainly in the work hardening characteristics, rather than the yield stress. The inferred plots were close to those obtained by conventional uniaxial compression testing (in the through-thickness direction), for both types of sample.

(d) It is concluded that the methodology has considerable potential for testing of materials (including coatings) in situations where conventional uniaxial testing is difficult or best avoided. The level of confidence that can be placed in outcomes is considered to be high, particularly if they are similar when using both load-displacement and residual indent profile data. Further information about the probable reliability is provided by the value of the goodness of fit parameter, which is used by the Nelder-Mead algorithm during convergence.

Acknowledgements

This work is supported by EPSRC (grant RG62695) and by the Leverhulme Trust. The latter support is in the form of an International Network grant (IN-2016-004) being used to promote a range of activities, including extensive Anglo-German collaboration - see https://www.ccg.msm.cam.ac.uk/initiatives/lincet. Funding has also been received from the Deutsche Forschungsgemeinschaft through the collaborative research center SFB/TR 103 on Single Crystal Superalloys, through project B6.

There has also been input from AWE, as part of an ongoing collaboration with the Gordon Laboratory in Cambridge, aimed at the development of robust and user-friendly tools for the extraction of mechanical property characteristics from instrumented indentation data. The authors are particularly grateful to Giles Aldrich-Smith, Nigel Park and Kevin Hunt, for extensive collaboration and support.

In compliance with current EPSRC recommendations, code and input data for the indentation modeling described here, including meshing and boundary condition specifications, are available at: www.ccg.msm.cam.ac.uk/publications/resources. The code is available at: github.com/rpt26/plasticity_extraction. It includes the convergence algorithm. These files can be downloaded and used with ABAQUS FEM models. Data supplied are for a representative case (with a spherical indenter and radial symmetry).

Appendix I. Nelder-Mead convergence algorithm

For a model with m parameters, searching is within an m-dimensional parameter space, within which a ***simplex*** is defined. This is a ***polytope*** with $(m+1)$ vertices (ie a triangle in 2-D, a tetrahedron in 3-D etc). Each vertex corresponds to a particular combination of all of the m parameters in the set and the simplex covers a range of values for all of these. These points can be expressed as vectors (first rank tensors) in parameter space, designated $\boldsymbol{x}_1$, $\boldsymbol{x}_2$, $\ldots\boldsymbol{x}_{m+1}$, each of which consists of a set of m parameter values. After each iteration (new set of FEM simulations), the objective is to "improve" the simplex by replacing the worst vertex (ie the one with the highest value of S) with a better point. The search for this better point is along a line in parameter space defined by the worst point and the centroid of the rest of the simplex, which is the average position of the remaining points (after removal of the worst point). Once an initial simplex has been created, each iteration comprises the following steps.

1 The values of S are calculated for each vertex and the vertices are ranked, such that $S(\boldsymbol{x}_1) < S(\boldsymbol{x}_2) < \ldots < S(\boldsymbol{x}_{m+1})$. The point to be replaced is $\boldsymbol{x}_{m+1}$. The centroid of the (reduced) simplex is calculated from:

$$x_{\text{cen}} = \frac{1}{m}\sum_{j=1}^{m} x_j \tag{A1}$$

This defines the search direction ($\boldsymbol{x}_{\text{cen}}$ - $\boldsymbol{x}_{m+1}$).

2 **Reflection**: A trial point is established by reflection of $\boldsymbol{x}_{m+1}$ through $\boldsymbol{x}_{\text{cen}}$.

$$x_{\text{ref}} = x_{\text{cen}} + \alpha(x_{\text{cen}} - x_{m+1}) \tag{A2}$$

where α is a scale factor. The value of S is calculated for this point. If $S(\boldsymbol{x}_1) < S(\boldsymbol{x}_{\text{ref}}) < S(\boldsymbol{x}_m)$, so that $\boldsymbol{x}_{\text{ref}}$ is of intermediate quality, then $\boldsymbol{x}_{\text{ref}}$ is accepted, replacing $\boldsymbol{x}_{m+1}$. Otherwise, the algorithm proceeds to step 3.

3 **Expansion**: If $S(\boldsymbol{x}_{\text{ref}}) < S(\boldsymbol{x}_1)$, so that $\boldsymbol{x}_{\text{ref}}$ is the best point yet, this could indicate that the simplex is on an extended downward gradient and an expanded point is trialed

$$x_{\text{exp}} = x_{\text{cen}} + \beta(x_{\text{cen}} - x_{m+1}) \tag{A3}$$

where β is a scale factor ($>\alpha$). . The value of S is calculated for this point. If $S(\boldsymbol{x}_{\text{exp}}) < S(\boldsymbol{x}_{\text{ref}})$, then $\boldsymbol{x}_{\text{exp}}$ is accepted, replacing $\boldsymbol{x}_{m+1}$. Otherwise, $\boldsymbol{x}_{\text{ref}}$ is accepted, replacing $\boldsymbol{x}_{m+1}$.

4 **Outside contraction**: If $S(\boldsymbol{x}_m) \le S(\boldsymbol{x}_{\text{ref}}) < S(\boldsymbol{x}_{m+1})$, so that $\boldsymbol{x}_{\text{ref}}$ is an improvement on $\boldsymbol{x}_{m+1}$, but would become the new worst point, the value of S Is calculated for a point between $\boldsymbol{x}_{\text{ref}}$ and $\boldsymbol{x}_{\text{cen}}$, called the outside contraction point.

$$x_{\text{OC}} = x_{\text{cen}} + \gamma(x_{\text{cen}} - x_{m+1}) \tag{A4}$$

where γ is a scale factor ($<\alpha$). The value of S is calculated for this point. If $S(\boldsymbol{x}_{OC}) \leq S(\boldsymbol{x}_{ref})$, then $\boldsymbol{x}_{OC}$ is accepted, replacing $\boldsymbol{x}_{m+1}$. Otherwise, the algorithm proceeds to step 6.

5 **Inside contraction**: If $S(x_{m+1}) \leq S(\boldsymbol{x}_{ref})$, so that $\boldsymbol{x}_{ref}$ is worse than all of the points in the existing simplex, then the value of S Is calculated for a point between $\boldsymbol{x}_{cen}$ and $\boldsymbol{x}_{m+1}$, called the inside contraction point.

$$x_{IC} = x_{cen} - \delta(x_{cen} - x_{m+1}) \tag{A5}$$

where δ is another scale factor. The value of S is calculated for this point. If $S(\boldsymbol{x}_{IC}) < S(\boldsymbol{x}_{ref})$, then $\boldsymbol{x}_{IC}$ is accepted, replacing $\boldsymbol{x}_{m+1}$. Otherwise, the algorithm proceeds to step 6.

6 **Shrink**: If none of the previous steps are able to improve the simplex, then it is shrunk towards the best vertex. This operation is defined by

$$x_j' = x_j + \delta(x_1 - x_j) \tag{A6}$$

for $2 \leq j\,(m+1)$. The algorithm then starts the next iteration at step 1.

The scale factors (α, β, γ and δ) are often ascribed values of 1, 2, 0.5 and 0.5 respectively, but these can be tuned to cope with particular situations, such as different levels of noise.

References

[1] K.L. Luthra, Low-temperature hot Corrosion of cobalt-base alloys 1. Morphology of the reaction product, Metall. Trans. A Metall. Phys. Mater. Sci. 13 (10) (1982) 1843–1852.
[2] N. Eliaz, G. Shemesh, R.M. Latanision, Hot corrosion in gas turbine components, Eng. Fail. Anal. 9 (1) (2002) 31–43.
[3] F. Pettit, Hot corrosion of metals and alloys, Oxid. Metals 76 (1–2) (2011) 1–21.
[4] P. Lortrakul, R.W. Trice, K.P. Trumble, M.A. Dayananda, Investigation of the mechanisms of Type-II hot corrosion of superalloy CMSX-4, Corrosion Sci. 80 (2014) 408–415.
[5] H. Singh, D. Puri, S. Prakash, An overview of Na2SO4 and/or V2O5 induced hot corrosion of Fe- and Ni-based superalloys, Rev. Adv. Mater. Sci. 16 (1–2) (2007) 27–50.
[6] M.N. Task, B. Gleeson, F.S. Pettit, G.H. Meier, The effect of microstructure on the type II hot corrosion of Ni-Base MCrAlY alloys, Oxid. Metals 80 (1–2) (2013) 125–146.
[7] P. Knutsson, H.P. Lai, K. Stiller, A method for investigation of hot corrosion by gaseous Na2SO4, Corrosion Sci. 73 (2013) 230–236.
[8] T. Gheno, B. Gleeson, On the hot corrosion of nickel at 700 a degrees C, Oxid. Metals 84 (5–6) (2015) 567–584.
[9] M. Gaumann, C. Bezencon, P. Canalis, W. Kurz, Single-crystal laser deposition of superalloys: processing-microstructure maps, Acta Mater. 49 (6) (2001) 1051–1062.
[10] R. Vilar, A. Almeida, Repair and manufacturing of single crystal Ni-based superalloys components by laser powder deposition-A review, J. Laser Appl. (2015) 27.
[11] Z.Y. Liu, H. Qi, L. Jiang, Control of crystal orientation and continuous growth through inclination of coaxial nozzle in laser powder deposition of single-crystal superalloy, J. Mater. Process. Technol. 230 (2016) 177–186.
[12] S. Kaierle, L. Overmeyer, I. Alfred, B. Rottwinkel, J. Hermsdorf, V. Wesling, N. Weidlich, Single-crystal turbine blade tip repair by laser cladding and remelting, CIRP Int. J. Manuf. Sci. Technol. 19 (2017) 196–199.
[13] J. Durocher, N.L. Richards, Evaluation of the low heat input process for weld repair of nickel-base superalloys, J. Mater. Eng. Perform. 20 (7) (2011) 1294–1303.
[14] X. Huang, W. Miglietti, Wide gap braze repair of gas turbine blades and vanes-a review, J. Eng. Gas. Turbines Power. Trans. ASME 134 (1) (2012).
[15] C. Churchman, E.A. Bonifaz, N.L. Richards, Comparison of single crystal Ni based superalloy repair by gas tungsten arc and electron beam processes, Mater. Sci. Technol. 27 (4) (2011) 811–817.
[16] J.Y. Sun, Y.L. Pei, S.S. Li, H. Zhang, S.K. Gong, Improved mechanical properties of Ni-rich Ni3Al coatings produced by EB-PVD for repairing single crystal blades, Rare Met. 36 (7) (2017) 556–561.
[17] K. Ogawa, T. Niki, Repairing of degraded hot section parts of gas turbines by cold spraying, in: M.H. Aliabadi, S. Abela, S. Baragetti, M. Guagliano, H.S. Lee (Eds.), Advances in Fracture and Damage Mechanics Viii, Trans Tech Publications Ltd: Stafa-Zurich, 2010, pp. 545–548.
[18] S. Vezzu, S. Rech, E. Vedelago, G.P. Zanon, G. Alfeo, A. Scialpi, R. Huang, On deposition of Waspaloy coatings by cold spray, Surf. Eng. 30 (5) (2014) 342–351.
[19] W.Y. Chan, H.E. Evans, C.B. Ponton, J.R. Nicholls, N.J. Simms, The influence of NiAl3 on the high temperature oxidation of a plasma-sprayed overlay coating, Mater. A. T. High. Temp. 17 (2) (2000) 173–178.
[20] K. Fritscher, Y.T. Lee, Investigation of an as-sprayed NiCoCrAlY overlay coating - microstructure and evolution of the coating, Mater. Corros. Werkstoffe Korrosion 56 (1) (2005) 5–14.
[21] M. Okazaki, I. Ohtera, Y. Harada, Damage repair in CMSX-4 alloy without fatigue life reduction penalty. Metallurgical and Materials Transactions a-Physical Metallurgy and Materials Science 35A (2) (2004) 535–542.
[22] H. Pelletier, Predictive model to estimate the stress-strain curves of bulk metals using nanoindentation, Tribol. Int. 39 (2006) 593–606.
[23] J. Isselin, A. Iost, J. Golek, D. Najjar, M. Bigerelle, Assessment of the constitutive law by inverse methodology: small punch test and hardness, J. Nucl. Mater. 352 (1–3) (2006) 97–106.
[24] C. Heinrich, A.M. Waas, A.S. Wineman, Determination of material properties using nanoindentation and multiple indenter tips, Int. J. Solid Struct. 46 (2009) 364–376.
[25] K. Bouzakis, N. Michailidis, An accurate and fast approach for determining materials stress-strain curves by nanoindentation and its FEM-based simulation, Materials Characterisation 56 (2006) 147–157.
[26] G. Bolzon, G. Maier, M. Panico, Material model calibration by indentation, imprint mapping and inverse analysis, Int. J. Solid Struct. 41 (11–12) (2004) 2957–2975.
[27] J. Dean, J.M. Wheeler, T.W. Clyne, Use of quasi-static nanoindentation Data to obtain stress-strain Characteristics for metallic materials, Acta Mater. 58 (2010) 3613–3623.
[28] V. Karthik, P. Visweswaran, A. Bhushan, D.N. Pawaskar, K.V. Kasiviswanathan, T. Jayakumar, B. Raj, Finite element analysis of spherical indentation to study pile-up/sink-in phenomena in steels and experimental validation, Int. J. Mech. Sci. 54 (1) (2012) 74–83.
[29] D.K. Patel, S.R. Kalidindi, Correlation of spherical nanoindentation stress-strain curves to simple compression stress-strain curves for elastic-plastic isotropic materials using finite element models, Acta Mater. 112 (2016) 295–302.
[30] J. Dean, T.W. Clyne, Extraction of plasticity parameters from a single test using a spherical indenter and FEM modelling, Mech. Mater. 105 (2017) 112–122.
[31] J.E. Campbell, R.P. Thompson, J. Dean, T.W. Clyne, Experimental and computational issues for automated extraction of plasticity parameters from spherical indentation, Mech. Mater. (2018) (in press).
[32] J.H. Hollomon, Tensile deformation, Trans. Am. Inst. Min. Metall. Pet. Eng. Inc. (AIME) 162 (1945) 268–290.
[33] A. Sengupta, S.K. Putatunda, L. Bartosiewicz, J. Hangas, P.J. Nailos, M. Peputapeck, F.E. Alberts, Tensile behaviour of a new single crystal nickel-based superalloy (CMSX-4) at room and elevated temperatures, J. Mater. Eng. Perform. 3 (5) (1994) 664–672.
[34] K. Demtroder, G. Eggeler, J. Schreuer, Influence of microstructure on macroscopic elastic properties and thermal expansion of nickel-base superalloys ERBO/1 and LEK94, Mater. Werkst. 46 (6) (2015) 563–576.
[35] K.F. Riley, M.P. Hobson, S.J. Bence, Mathematical Methods for Physics and Engineering, third ed. Set ed, Cambridge University Press, 2006.
[36] J.A. Nelder, R. Mead, A simplex Method for function minimization, Comput. J. 7 (4) (1965) 308–313.
[37] F.C. Gao, L.X. Han, Implementing the Nelder-Mead simplex algorithm with adaptive parameters, Comput. Optim. Appl. 51 (1) (2012) 259–277.